



CHORUS

This is the accepted manuscript made available via CHORUS. The article has been published as:

Atomic Structure of Highly Strained BiFeO₃ Thin Films

M. D. Rossell, R. Erni, M. P. Prange, J.-C. Idrobo, W. Luo, R. J. Zeches, S. T. Pantelides, and
R. Ramesh

Phys. Rev. Lett. **108**, 047601 — Published 24 January 2012

DOI: [10.1103/PhysRevLett.108.047601](https://doi.org/10.1103/PhysRevLett.108.047601)

Atomic Structure of Highly Strained BiFeO₃ Thin Films

M. D. Rossell,^{1,2,*} R. Erni,¹ M. P. Prange,^{3,4} J.-C. Idrobo,^{4,3} W. Luo,⁵ R. J. Zeches,⁶ S. T. Pantelides,^{3,4} and R. Ramesh^{6,7,8}

¹*Electron Microscopy Center, Empa, Swiss Federal Laboratories for Materials Science and Technology, CH-8600 Dübendorf, Switzerland*

²*Department of Materials, ETH Zürich, CH-8093 Zürich, Switzerland*

³*Department of Physics and Astronomy, Vanderbilt University, Nashville, Tennessee 37235, USA*

⁴*Materials Science and Technology Division, Oak Ridge National Laboratory, Oak Ridge, Tennessee 37831, USA*

⁵*Geballe Laboratory for Advanced Materials, Stanford University, Stanford, California 94305, USA*

⁶*Department of Physics, University of California, Berkeley, California 94720, USA*

⁷*Materials Sciences Division, Lawrence Berkeley National Laboratory, California 94720, USA*

⁸*Department of Material Science and Engineering, University of California, Berkeley, California 94720, USA*

We determine the atomic structure of the pseudotetragonal T-phase and the pseudorhombohedral R-phase in highly strained multiferroic BiFeO₃ thin films by using a combination of atomic-resolution scanning transmission electron microscopy and electron energy-loss spectroscopy (EELS). The coordination of the Fe atoms and their displacement relative to the O and Bi positions are assessed by direct imaging. These observations allow us to interpret the electronic structure data derived from EELS and provide evidence for the giant spontaneous polarization in strained BiFeO₃ thin films.

PACS numbers: 77.55.Nv, 77.65.Ly, 68.37.-d, 79.20.Uv

Due to their astounding electromechanical properties, BiFeO₃ (BFO) thin films are promising candidates for the replacement of lead-based ceramics in MEMS devices. However, a full understanding of the piezoelectric properties reported for these ceramic materials [1, 2] is still missing. Detailed knowledge about the crystal structure of BFO thin films in all its polymorphic structures is of essential importance to address this lack.

While the structure of the “bulk” BFO phase has already been determined by neutron [3] and x-ray crystallography [4], polymorphs of BFO stabilized under epitaxial strain are not yet fully understood. Two distinct structures are known to evolve above and below a 4.5% critical compressive strain. They are pseudotetragonal (T-phase) and pseudorhombohedral (R-phase), respectively, with a small monoclinic distortion of the unit cells [5, 6]. The T-phase shows a unique structure characterized by a strongly elongated unit cell with a c/a axial ratio (ratio of the long to short axis of the pseudocubic unit cell) close to 1.3. The structural information of this metastable polymorph is particularly relevant because it is predicted to have a giant polarization as high as 150 $\mu\text{C}/\text{cm}^2$ [6–8], roughly 1.5 times of the bulk material. This theoretical result has also been confirmed experimentally [9], and more recently by Zhang *et al.* [10].

The T-phase can only be prepared either as pure-phase in highly strained films thinner than 50 nm grown on LaAlO₃ substrates [11] or as a nanoscale mixture of T- and R-phases in partially relaxed films [5, 12–14]. Due to these limitations, obtaining experimental data about the atomic and electronic structure of the T-phase is very challenging. As a matter of fact, detailed crystal structure determination of the high strain BFO polymorph

has only been accessible via theoretical calculations. Indeed, the stabilization of a metastable phase in BFO films under high compressive epitaxial strain was first found by theoretical studies [7, 8]. They anticipated the high-strain BFO polymorph would exhibit a tetragonal $P4mm$ symmetry with a c/a ratio of ~ 1.27 accompanied by a large Fe displacement towards one of the apical oxygens along $[001]_{pc}$ (where pc denotes pseudocubic indices) resulting in five-fold oxygen coordinated Fe, similar to the square-pyramidal coordination of the transition metals in PbVO₃ [15] and BiCoO₃ [16]. Later on, an antiferrodistortive tilting of the square-pyramidal oxygen cages (analogous to the octahedral tilt) by 5.1° around $[110]_{pc}$ was foreseen to break the tetragonal symmetry [6], allowing switching the polarization vector. Besides, the ferroelectric polarization of the T-phase structure is also under debate. While several groups have described the Fe off-center displacement to be unique along the out-of-plane direction [5, 12], a strong in-plane component on T-phase domains in films grown on LaAlO₃ and LaSrAlO₄ substrates has been detected [13, 14, 17].

In this Letter we report direct measurements of the atomic and electronic structure of this intriguing high-strain T-phase by comparison to the low-strain R-phase. We present an atomic-resolution study using aberration-corrected high-angle annular dark-field scanning transmission electron microscopy (HAADF-STEM) [18] and EELS in combination with first-principle density functional theory calculations, and multiple-scattering calculations of the energy-loss near-edge structure (ELNES) [19, 20]. Details of the experimental and computational techniques are given in the Supplemental Material [21].

A 60-nm-thick BFO film grown on LaAlO₃ was used

for STEM. The film consists of a nanoscale mixture of the T- and R-polymorphs shown in Fig. 3(a) as bright and dark bands due to residual coherent diffraction contrast. A high-resolution STEM (HRSTEM) image of the BFO thin film is shown in Fig. 1(a). It corresponds to a slab of the T-phase (center) embedded in R-phase matrix. In accordance with earlier electron microscopy studies [12], a smooth transition with defect-free interfaces is observed between both phases. By analyzing the HRSTEM image by geometric phase analysis (GPA) [22], we determined the local deformation and rotation of the lattice fringes. The deformation of the lattice spacing was determined relative to an internal reference lattice selected at the bottom left side of the image. Quantitative measurements of the crystallographic lattice deformation by the GPA method are presented in Figs. 1(c)- 1(f). These results were calculated by choosing the spots indicated as $\mathbf{g}_1 = 100$ and $\mathbf{g}_2 = 001$ in the power spectrum given in Fig. 1(b). Artifacts due to line-to-line scanning errors of the HAADF-STEM image are perceptible as horizontal stripes in Figs. 1(d) and 1(e). These fluctuations are absent in Figs. 1(c) and 1(f) because the scanning direction is parallel to the principal axis of the strain. However, despite the presence of scanning errors, GPA could be successfully used as an effective reproducible technique to quantitatively measure the local strain at the morphotropic phase boundaries (MPBs). Figures 1(c) and 1(d) show the change in lattice spacing perpendicular and parallel to the growth axis, respectively. For this specific area, the T-phase (central slab) as compared to the R-phase structure is slightly smaller in the in-plane direction ($-3.2 \pm 0.9\%$) but $16.7 \pm 2.0\%$ larger in the out-of-plane direction. The rotation maps in Figs. 1(e) and 1(f) show the rotation of the lattice fringes with respect to the parallel and the perpendicular to the growth axis, respectively. The rotation is chosen positive anticlockwise. Thus, Figs. 1(e) and 1(f) reveal an average rigid rotation angle $\Delta\Omega$ of $3.8^\circ \pm 1.1^\circ$ and $4.2^\circ \pm 0.6^\circ$ between the adjacent phases. These results are in good agreement with the sum of tilt angles of $\sim 2.8^\circ$ and $\sim 1.6^\circ$ derived from x-ray [23, 24] and electron diffraction [24].

It was previously reported that the deformations at the MPB interface are confined to a distance of 10 unit cells [12]. However, our current analysis (repeated at various areas of the sample) unveils that these boundaries exhibit slightly different behavior depending on their location with respect to the T-phase slab. Thus, a smoother transition taking place over up to 20 unit cells is observed for the phase boundary located at the left side of the slab, while the transition appears to occur abruptly (in only 4-5 unit cells) at the boundary located closer to the film surface.

Figures 2(a) and 2(b) show HRSTEM images of the R- and T-phases in the $[010]_{pc}$ orientation, respectively. Figure 2(b) demonstrates a strong tetragonal distortion of the cubic perovskite. The measured axial ratio c/a

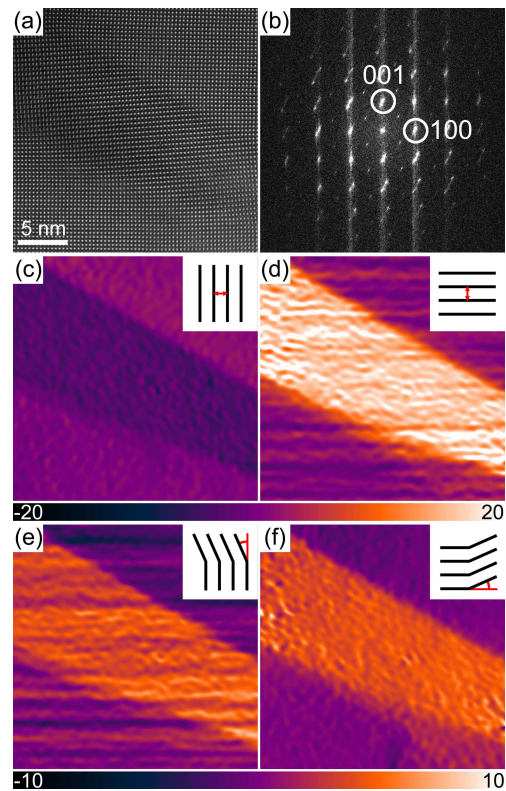


FIG. 1. (Color online) Morphotropic phase boundaries in a BFO film analyzed with GPA. (a) HRSTEM cross-sectional image. The film growing direction is bottom to top. (b) Corresponding Fourier transform. (c) In-plane and (d) out-of-plane strain fields. The color bar below gives the change in lattice spacing relative to the reference lattice in %. [(e) and (f)] Rigid lattice rotation maps. The corresponding color bar gives the rigid rotation angle $\Delta\Omega$ in deg. The insets show a schematic representation of the lattice deformations measured in each map.

for the T-phase is 1.27, in comparison to 1.03 for the R-phase. In the low-strain R-phase structure, the Fe atoms are displaced from the center of the oxygen octahedra along $[111]_{pc}$, forming short and elongated Fe-O bonds [Fig. 2(a)] [25]. Nevertheless, the Fe cation keeps the three-dimensional framework of octahedra. However, the extreme c -parameter elongation of the T-phase structure is connected with the transformation of the FeO_6 octahedra into FeO_5 pyramids [Fig. 2(b)]. The off-center displacement of Fe with respect to Bi was measured from several micrographs to be mainly out-of-plane ($6.3 \pm 1.0\%$) although a small in-plane component of $2.0 \pm 1.3\%$ was observed as well. Note that these are values of the measured projection of the Fe off-center displacement onto the $(010)_{pc}$ plane.

In order to gain detailed atomic-scale structural information from both BFO polymorphs present in the film, we derived averaged structures [21] from the HRSTEM images in Figs. 2(a) and 2(b). These averaged structures, obtained from areas containing 150 unit cells, are

shown as insets. Due to the limited dynamical range of the detection process and the presence of shot noise it is very difficult to directly image the light oxygen columns in $[010]_{pc}$ -orientation above the background intensity between the heavy Bi ($Z = 83$) and FeO ($Z = 26$; 8) columns. This is even more complicated in the case of the R-phase as the neighboring octahedral oxygen cages, along the electron-beam direction, rotate in opposite directions. Thus, the oxygen atoms are not aligned in a single column of atoms but rather forming a zig-zag structure along the beam direction which results in a different electron channelling condition that effectively reduces the image intensity of the oxygen atoms; see the yellow oxygen atoms in the model in Fig. 2(a). However, visualization of the oxygen positions is possible when the oxygen atoms are aligned in a single column of atoms as in the case of the T-phase. The averaged T-phase structure of Fig. 2(b) reveals the presence of distinct intensity maxima right below the large Bi atomic columns. These maxima correspond to equatorial O(2) oxygen atomic columns displaced upwards to maintain the five-fold oxygen coordination about the displaced Fe atoms; see the white oxygen atoms in the model in Fig. 2(b). An intensity profile taken across the Bi and O(2) atomic columns in the averaged T-phase structure is shown in Fig. S1. The iron atom is shifted by $\sim 0.7 \text{ \AA}$ from the square plane formed by four O(2) equatorial oxygen atoms towards the vertex of the pyramid (yellow apical O(1) oxygen atoms), forming a short Fe-O(1) bond. The measured Fe-O(2) separation, assuming the a and b parameters are equivalent, is $1.98 \pm 0.04 \text{ \AA}$. In good agreement with the image simulation, the apical O(1) oxygen atoms could not be resolved as they are not aligned along the electron-beam direction due to the oxygen square-pyramidal tilts. Finally, the Bi atoms are shifted towards one of the equatorial oxygen planes as the result of the influence of the lone pair, located opposite to the shift direction due to steric factor. Therefore, half of the Bi-O(2) distances become noticeably shorter, $2.33 \pm 0.04 \text{ \AA}$, than the other ones ($3.78 \pm 0.04 \text{ \AA}$), which can be considered as nonbonding. We have performed first-principles density functional theory calculations using the measured lattice constants of the T-phase structure. The calculated atomic positions agree well with the experimental measurement. Using the calculated Born effective charge tensors, we obtain the out-of-plane component of the polarization to be $148 \mu\text{C}/\text{cm}^2$ [21], confirming the giant spontaneous polarization in the T-phase structure of BiFeO_3 .

Epitaxial strain has also important consequences on the local electronic structure of BFO films. To get more insight into this intriguing high-strain T-phase, we performed EELS measurements at the Fe $L_{3,2}$ and the O K -edges. Analogous measurements were obtained from the low-strain R-phase for comparison. Figure 3(a) shows a low magnification STEM cross-sectional image of a BFO film consisting of a nanoscale mixture of T-phase (regions

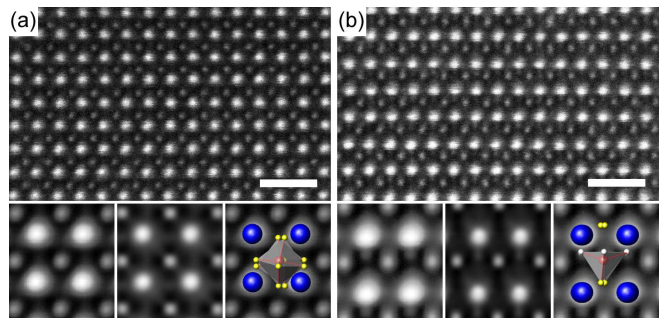


FIG. 2. (Color online) [(a) and (b)] Atomic resolution HAADF-STEM images of the R- and T-phase, respectively. Insets below, from left to right: averaged structure images; simulated STEM images for a 50 nm thick crystal; and averaged structure images with overlaid structure models. Blue, red and yellow spheres represent Bi, Fe and oxygen atoms, respectively. For the T-phase model, the equatorial O(2) oxygen atoms are shown in white to differentiate them from the yellow apical O(1) oxygen atoms. The scale bars are 1 nm.

II and IV) and R-phase (regions I and III). The EELS spectra in this study were obtained from the regions indicated as I-IV in Fig. 3(a). During acquisition of the experimental spectra the probe was scanned in a small frame located on one of the phases in order to reduce possible beam damage. Thus, the experimental results reflect the integral of all possible oxygen environments in each phase. As expected, the spectra obtained from regions II and IV corresponding to the T-phase are equivalent. Similarly, the spectra obtained from regions I and III of the R-phase are also equivalent.

The oxygen K -edge spectrum of the BFO phases shown in Fig. 3(b) can be divided into two sections, a pre-peak region from 531 to 538 eV and a post-edge peak from 538 to 548 eV. The pre-peak region contains two dominant peaks at 533.5 eV (labeled A1) and a smaller one at 536 eV (labeled A2). The first section involving the first 4 eV above the threshold (peak A1) was previously identified as resulting from hybridization between the O $2p$ and Fe $3d$ states. On the other hand, the A2 peak stems from transitions to hybridized O $2p$ -Bi $5d$ orbitals [26] or possibly also O $2p$ -Bi $6d$ (-Bi $5d$) orbitals [27]. Thus, in these strained BFO phases the A1 and A2 peaks are not due to crystal-field splitting in BFO. The crystal-field splitting is contained mainly within peak A1 [27]. Here, at an energy resolution of 0.6 eV [21], we can barely resolve the shoulder located on the left side of the A1 peak. The most striking difference between the spectra of the R- and T-phases is found in the post-edge region. In this region the R-phase spectrum shows two well-defined peaks at 541.3 eV (labeled B1) and at 543.5 eV (labeled B2). On the contrary, the T-phase spectrum contains a single B1 peak at 541 eV, while no B2 peak is observed. The covalent oxygen-transition metal bond in this range is well known for both transition metal oxides

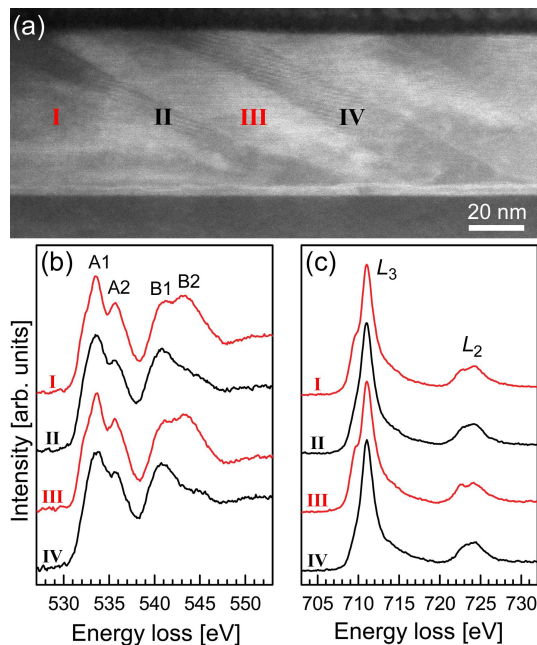


FIG. 3. (Color online) (a) Low magnification STEM cross-sectional image of a BFO film on a LaAlO_3 substrate consisting of a nanoscale mixture of T-phase (regions II and IV) and R-phase (regions I and III). (b) Oxygen K -edge and (c) iron L -edge spectra of the areas indicated in (a).

[28, 29] and perovskites [30, 31]. The peak B stems from the transitions to hybridized O $2p$ and Fe $4sp$ states and is related to the local coordination of the Fe atoms set up by the nearest oxygen neighbors. Therefore, the differences observed in the B features of the R- and T-phase spectra indicate differences in the Fe-O bonding due to different coordination geometries for the Fe atoms. This observation corroborates the atomic structure information derived from STEM. Besides, our experimental EELS data was complemented with calculations of the ELNES of the oxygen K -edge. The theoretical data, which is given in the Supplemental Material [21] qualitatively confirm the experimental data.

Figure 3(c) shows the Fe $L_{3,2}$ edge of the T-phase (labeled II and IV) and the R-phase (labeled I and III). The Fe $L_{3,2}$ edge corresponds to excitations from the Fe $2p$ electrons ($2p^63d^5$) into empty Fe $3d$ states ($2p^53d^6$). These transitions produce two main features, the so-called “white-lines”, at 710 eV (Fe $2p_{3/2} \rightarrow$ Fe $3d$) and 723 eV (Fe $2p_{1/2} \rightarrow$ Fe $3d$) that are separated by 12.9 eV due to spin-orbit splitting of the Fe $2p$ core hole into $2p_{3/2}$ and $2p_{1/2}$ states. Besides, extra fine structures appearing as shoulders on the left side of the white-lines can be observed in the spectra of the R-phase. This further splitting of the $3d$ orbital states into t_{2g} and e_g levels is due to the octahedral crystal field. The measured energy separation between t_{2g} and e_g states is 1.4 eV.

For the T-phase the crystal-field splitting could not be

resolved experimentally. The reason being that in the high-strain T-phase one of the oxygen atoms is moved to a nonbonding distance transforming the octahedron into a square pyramid with four reduced equatorial Fe-O(2) bonds and a shorter apical Fe-O(1) bond [6]. These modifications split the t_{2g} states into a doubly-degenerate pair (d_{xz}, d_{yz}) and a singly-degenerate d_{xy} level (with the d_{xy} state at a higher energy than the d_{xz}, d_{yz} pair). Similarly, the e_g states break symmetry to yield a lower energy d_{z^2} state and a higher energy $d_{x^2-y^2}$ level. However, owing to the limited energy resolution of our experimental setup, it was not possible to resolve these four different states resulting in a broadening of the T-phase white lines. Our calculations [21] confirm this trend predicting that the unoccupied Fe $3d$ states broaden in the quasi-tetragonal system. These results are in excellent agreement with band structure calculations reported previously [8, 32].

In conclusion, by using aberration-corrected HAADF-STEM imaging, we find that the high-strain and low strain BFO polymorphs exhibit substantial differences in their atomic crystal structure. Our results provide direct experimental evidence for the square-pyramidal oxygen coordination of the iron atoms in the high-strain T-phase. We have shown that the iron and the equatorial oxygen atomic columns can be directly imaged in the T-phase, confirming that they are significantly displaced along the c -direction. Besides, by comparing our HRSTEM experimental results with simulations we corroborate the theoretical calculations suggesting antiferrodistortive tilting of the square-pyramidal oxygen cages around $[110]_{pc}$ [6]. Moreover, the Fe atom displacement relative to the Bi atoms was found to be both along the out-of-plane and in-plane directions. From the measured ionic displacements a giant out-of-plane ferroelectric polarization ($148 \mu\text{C}/\text{cm}^2$) and a small in-plane polarization ($13 \mu\text{C}/\text{cm}^2$) are estimated, in excellent agreement with previous theoretical results [6]. We have shown that these modifications, in turn, have a direct impact on the electronic structure of BFO resulting in clear differences in the near-edge fine structure of the O K - and Fe $L_{3,2}$ -edges. Thus, the results presented clarify the microscopic origin of the giant ferroelectric polarization measured in these multiferroic thin films.

We gratefully acknowledge Alison Hatt and Nicola Spaldin for providing the structural models and for useful discussions. We acknowledge financial support of the Swiss COST office under the SBF project number C10.0089 (MDR, RE); the Oak Ridge National Laboratory’s SHaRE User Facility (JCI), which is sponsored by the Office of Basic Energy Sciences, U.S. Department of Energy; the Office of Basic Energy Sciences, Materials Sciences and Engineering Division, U.S. Department of Energy under contract number DE-FG02-09ER46554 (MPP, STP); and the McMinn Endowment (STP) at Vanderbilt University. This research used resources of the National Center for Electron Microscopy (LBNL) and

the National Energy Research Scientific Computing Center, which are supported by the Office of Science, Office of Basic Energy Sciences of the U.S. Department of Energy under contract number DE-AC02-05CH11231.

* marta.rossell@empa.ch

- [1] J. X. Zhang *et al.*, Nature Nanotech. **6**, 98 (2011).
 [2] H. Béa *et al.*, J. Phys.: Condens. Matter **23**, 142201 (2011).
 [3] P. Fischer *et al.*, J. Phys. C.: Solid St. Phys. **13**, 1931 (1980).
 [4] F. Kubel and H. Schmid, Acta Crystallogr. B **46**, 698 (1990).
 [5] H. Béa *et al.*, Phys. Rev. Lett. **102**, 217603 (2009).
 [6] A. J. Hatt, N. A. Spaldin, and C. Ederer, Phys. Rev. B **81**, 054109 (2010).
 [7] C. Ederer and N. A. Spaldin, Phys. Rev. B **71**, 060401 (2005).
 [8] D. Ricinchi, K.-Y. Yun, and M. Okuyama, J. Phys.: Condens. Matter **18**, L97 (2006).
 [9] K. Y. Yun *et al.*, Appl. Phys. Lett. **89**, 192902 (2006).
 [10] J. X. Zhang *et al.*, Phys. Rev. Lett. **107**, 147602 (2011).
 [11] C.-J. Cheng *et al.*, Appl. Phys. Lett. **98**, 242502 (2011).
 [12] R. J. Zeches *et al.*, Science **326**, 977 (2009).
 [13] D. Mazumdar *et al.*, Nano Lett. **10**, 2555 (2010).
 [14] Z. H. Chen *et al.*, Adv. Funct. Mater. **21**, 133 (2011).
 [15] R. V. Shpanchenko *et al.*, Chem. Mater. **16**, 3267 (2004).
 [16] A. A. Belik *et al.*, Chem. Mater. **18**, 798 (2006).
 [17] Z. H. Chen *et al.*, Appl. Phys. Lett. **96**, 252903 (2010).
 [18] R. Erni *et al.*, Phys. Rev. Lett. **102**, 096101 (2009).
 [19] J. J. Rehr and R. C. Albers, Phys. Rev. B **41**, 8139 (1990).
 [20] J. J. Rehr *et al.*, C. R. Physique **10**, 548 (2009).
 [21] See Supplemental Material. . . .
 [22] M. J. Hÿtch, E. Snoeck, and R. Kilaas, Ultramicroscopy **74**, 131 (1998).
 [23] Q. He *et al.*, Nat. Commun. **2**, 225 (2010).
 [24] Z. Chen *et al.*, Phys. Rev. B **84**, 094116 (2011).
 [25] J. B. Neaton *et al.*, Phys. Rev. B **71**, 014113 (2005).
 [26] K. Y. Yun *et al.*, J. Phys. Chem. C **112**, 10359 (2008).
 [27] R. Sæterli *et al.*, Phys. Rev. B **82**, 064102 (2010).
 [28] Z. Y. Wu *et al.*, Phys. Rev. B **55**, 2570 (1997).
 [29] F. M. F. de Groot *et al.*, Phys. Rev. B **40**, 5715 (1989).
 [30] F. M. F. de Groot *et al.*, Phys. Rev. B **48**, 2074 (1993).
 [31] N. D. Browning, H. O. Moltaji, and J. P. Buban, Phys. Rev. B **58**, 8289 (1998).
 [32] H. M. Tütüncü and G. P. Srivastava, Phys. Rev. B **78**, 235209 (2008).